ROYAL SOCIETY OF CHEMISTRY

PAPER

Check for updates

Exploring compositional versatility of perovskite-like Cs₃(Bi,Sb)₂X₉ (X = Cl, Br, I) compounds by high-throughput experimentation†

Oleksandr Stroyuk, [ID] *[a] Oleksandra Raievska,[a] Sachin Kinge,[b] Jens Hauch[ac] and Christoph J. Brabec[ac]

A high-throughput compositional screening of perovskite-like $Cs_3M_2X_9$ double salts (M = Bi and Sb and X = Cl, Br, and I) allows independent variation of the M and X components, yielding one hundred single-phase products within a general synthetic approach that combines engineered precipitation of chloride and bromide precursors and their anion exchange conversion into more complex halide derivatives. The X variation at a fixed M = Bi^{3+} yields various single-phase $Cs_3Bi_2X_9$ compounds with X = Cl, Cl + Br, Br, Br + I, and Cl + Br + I. The anion exchange in chlorides with Br + I combinations produces stable $Cs_3Bi_2X_9$ compounds with all three halides simultaneously present in the lattice, and Cl, Br, and I contents varied in the ranges of *ca.* 40–90%, 10–60%, and 30–90%, respectively. The presence of bromide, even as a residue, enables the co-existence of Cl and I, and dictates the trigonal symmetry, in contrast to the hexagonal symmetry typical for $Cs_3M_2I_9$. The compounds with X = Cl + Br + I show band gap variations in the range of 2.0–2.5 eV and linear dependencies on the iodide content and lattice parameters. The simultaneous variation of the X and M sites yields single-phase $Cs_3(Bi,Sb)_2X_9$ solid-solution compounds with tailorable X and a Bi/Sb ratio varied from 0 to 1.0. All Bi/Sb families reveal a band bowing effect, with the band gaps of mixed Bi/Sb compounds being lower than those of Bi- and Sb-only counterparts. The bowing parameter depends on the X subsystem, decreasing from 0.80 eV for Cl to 0.60 eV for Cl + Br and 0.40–0.45 eV for Br and Br + I, indicating that chemical variations in the mixed Bi/Sb lattices, rather than local disorders or lattice strains, govern the band-bowing behavior.

1 Introduction

Lead-free halide perovskites came into the research spotlight as potential alternatives to lead halide perovskites that showed enormous potential as emerging photovoltaic (PV) absorbers, developing with unprecedented speed into a competitor to traditional silicon PV absorbers.[1,2] In recent years, the studies of lead-free halide perovskites have formed an independent research direction targeting numerous potential applications far beyond PV and exploiting the unique compositional and

structural variability of these compounds.[3–5] The compositional versatility of lead-free halide perovskites stems not only from a variety of mono-, bi, tri, and tetravalent cations that can be accommodated in different crystallographic positions of the perovskite framework, but also from its high tolerance to multiple alloyings, substitutions, and dopings.[3,4,6]

The vast compositional space of lead-free halide perovskites is further expanded by their structural diversity, including "classical" $AM^{II}X_3$ perovskites (where A and M are cations and X is a halide), double $A_2M^IM^{III}X_6$ perovskites, 2D perovskites, vacancy-ordered $A_2M^{IV}X_6$ perovskites, perovskite-like $A_3M^{III}_2X_9$ double salts, *etc.*[3,4]

Halide perovskite-like lead-free double salts $A_3M_2X_9$, such as $Cs_3Bi_2I_9$ or $Cs_3Sb_2Br_9$, are recognized for their high stability and potential for applications in photodetection,[6–9] PV,[10,11] photocatalysis,[12–14] supercapacitors[15] and memory devices.[16,17] Like bismuth (antimony) double perovskites, Bi(Sb) double salts can accommodate alloyings, substitutions, and dopings, providing three crystallographic sites for independent compositional variation. The A site is typically occupied by Cs, but can also host Rb^{18} or methylammonium,[19,20] the M position combines Bi and

[a] Forschungszentrum Jülich GmbH, Helmholtz-Institut Erlangen Nürnberg für Erneuerbare Energien (HI ERN), 91058 Erlangen, Germany
[b] Materials Engineering Div., Toyota Motors Europe, Belgium.
  E-mail: sachin.kinge@toyota-europe.com
[c] Friedrich-Alexander-Universität Erlangen-Nürnberg, Materials for Electronics and Energy Technology (i-MEET), Martensstrasse 7, 91058 Erlangen, Germany

† Electronic supplementary information (ESI) available: Details on materials, methods, and synthesis of samples; tabulated summary of selected structural and spectral parameters of $Cs_3(Bi,Sb)_2X_9$ compounds; photographs of sample arrays; additional XRD and SEM data; analysis of absorption spectra of Bi/Sb mixed compounds. See DOI: https://doi.org/10.1039/d5ma00479a

Sb,[20–22] and the X component can be filled by individual halides or combinations of $Cl + Br$[13] and $Br + I$.[9,14,16]

While the synthesis conditions typically pre-define the A and M positions, the halide X position can be flexibly and broadly tuned by post-synthetic anion-exchange procedures. This approach was initially developed for lead–halide compounds[23–28] and then adapted for the compositional variations of lead-free perovskites[29–34] and perovskite-like double salts.[8,9,19,35–39]

Double salts with alloyed X or M components often show advanced functional characteristics, providing arguments for compositional screening. For example, mixed-halides such as $Cs_3Bi_2(Br,I)_9$[14] and $Cs_3Sb_2(Cl,Br)_9$[13] showed much higher photocatalytic activity in CO_2 photoreduction as compared to the corresponding individual halides. Alloyed $Cs_3Bi_2(Br,I)_9$ single crystals are more sensitive to X-rays than simpler bromide and iodide counterparts.[9] Similar effects of the M^{III} site composition on the functional properties were reported for Bi/Sb alloying, in particular, for $MA_3(Bi_{0.5}Sb_{0.5})_2I_9$, showing a higher PV activity than Bi-only and Sb-only counterparts.[20]

Still, as compared to the state-of-the-art in the research of double lead-free perovskites, the potential of the compositional variability of $A_3M_2X_9$ double salts seems to be under-evaluated, leaving much space for further exploration. Partially, this deficiency comes from limitations of the synthetic approaches, typically applied to produce $A_3M_2X_9$ compounds, such as high-temperature alloying of halides,[9] hydrothermal synthesis,[22] and ultrasonic[37] or mechanochemical treatments.[35,40] Being effort- and energy-intensive, these methods are hard to adapt for a broad compositional screening of a large number of double salts, also providing only a limited control over the phase purity and composition of the final products.

Recently, we have reported a high-throughput (HTP) approach for the screening of $Cs_2Ag_xNa_{1-x}M^{III}Cl_6$ double perovskites with M^{III} composed of two or three different trivalent metals, including compounds with $M^{III} = Bi + In$ (abbreviated as CANBIC by the first letters of constituent elements), $Bi + Sb$ (CANBSC), $Sb + In$ (CANSIC), $Bi + In + Sb$ (CANBISC), and $Bi + In + Fe$ (CANBIFC).[41] These compounds were produced using a general open-atmosphere precipitation protocol as single-phase sample families with independently varied Na/Ag and M^{III} ratios.

Along with the "green" room temperature synthesis of chloride double perovskites, a comparably mild procedure was developed for their conversion into bromide and iodide derivatives using stable and affordable NaBr and NaI as anion-exchange agents.[32] Originally tested on $Cs_2AgBi_xSb_{1-x}Cl_6$ (CABSC) perovskites,[32] this anion-exchange-based procedure can be applied to all above-discussed families of double chloride elpasolites, potentially opening the way for a much broader assortment of perovskite materials with varied band gaps.

However, a systematic screening of the products of such anion exchanges showed that most of the products were multi-phase mixtures, either due to the instability of corresponding bromide and iodide double perovskites, as in the case of CANBIC or CANSIC, or due to redox reactions between M^{III} species and bromide/iodide anions, as in the case of iron-based perovskites. One of a few cases of single-phase products of the anion-exchange-driven transformations of chloride double perovskites is the family of the perovskite-like $Cs_3(Bi, Sb)_2X_9$ double salts with tunable Bi/Sb ratios and variable compositions of the X site. Though being a product of serendipity on the way to bromide and iodide double perovskites, such double salts revealed a relatively large and still unreported compositional variability, thus constituting a promising research topic.

The present report illustrates the compositional variability of $Cs_3M_2X_9$ compounds by mixing chloride, bromide, and iodide anions on the X site and simultaneously combining Bi^{3+} and Sb^{3+} on the M site, and all compositions precipitated as single-phase products with the same structural motif.

2 Results and discussion

2.1 General motivation

As mentioned in the Introduction section, our recent HTP screening campaign was focused on chloride elpasolites with up to 6 metal cations, yielding a set of $Cs_2(Ag,Na)M^{III}Cl_6$ compounds with $M^{III} = Bi + In$, $Bi + Sb$, $Sb + In$, $Bi + Sb + In$, and $Bi + In + Fe$.[41]

These sample arrays were subjected to a mild anion exchange reaction with NaBr or NaI, converting chloride elpasolites into corresponding bromide or iodide derivatives, as reported earlier for $Cs_2AgBi_xSb_{1-x}Cl_6$ perovskites.[32] All experimental details, including the descriptions of syntheses, post-synthetic purifications, and anion exchanges, as well as details of the characterization, are presented in the ESI.†

A visual inspection of the anion-exchanged samples shows clear signs of the formation of bromide and iodide derivatives (see exemplary photographs in the ESI,† Fig. S1). However, a structural inspection of most of the samples using powder X-ray diffraction (XRD) reveals them to be complex multi-phase mixtures (ESI,† Fig. S2–S4), but not the desired bromide or iodide double perovskites. In particular, CANBIC perovskites (ESI,† Fig. S1a) treated with NaBr decompose into complex mixtures of $Cs_2NaInCl_6$ and $Cs_2AgBiBr_6$ double perovskites, $Cs_3Bi_2Br_9$ double salt (further denoted as CB–B), and AgBr (structural data available but not shown). Even the simpler case of sodium-only CNBIC double perovskites yields two phases, $Cs_2NaInCl_6$ and CB–B (ESI,† Fig. S2a), with the double salt content linearly depending on the Bi fraction in the original CNBIC perovskites (ESI,† Fig. S2b). Similarly, the interaction of CNBIC compounds with NaI also results in their decomposition and formation of $Cs_2NaInCl_6$ perovskites and $Cs_3Bi_2I_9$ (CB–I) double salts (ESI,† Fig. S3a), the amount of CB–I being proportional to the Bi fraction in the original CNBIC compounds (ESI,† Fig. S3b).

Similar to the anion exchange of CANBIC perovskites, the anion exchange of CANBSC perovskites (ESI,† Fig. S1b) with NaBr gives mixtures of $Cs_2Ag(Bi,Sb)(Cl,Br)_6$ perovskites, $Cs_3(Bi,Sb)_2(Cl,Br)_9$ double salts (denoted as CBS–CB), and residual AgBr (ESI,† Fig. S4). Such transformations were observed for all silver-containing compositions (series B to F in the CANBSC sample array, ESI,† Fig. S1b) and discussed in detail elsewhere.[32]

A detailed XRD analysis of row A in the CANBSC array (zero silver content) revealed it to be a family of $Cs_3(Bi,Sb)_2Cl_9$ double salts (CBS–C), rather than the expected CNBSC double perovskites.[41] In contrast to silver-containing samples, the Cl-to-Br exchanges in CBS–C yielded single-phase CBS–CB double salts with a variable Bi/Sb ratio (ESI,† Fig. S4a).

The anion exchanges of all CANBSC perovskites with NaI produce AgI and $Cs_3(Bi,Sb)_2I_9$ double salts (denoted as CBS–I) with a variable Bi/Sb ratio (see exemplary series A in the ESI,† Fig. S4b). Both CBS–CB and CBS–I compounds are discussed in the next sections.

The anion-exchange-driven transformations of more complex double perovskites, with M^{III} = Sb + In, Bi + In + Sb, and Bi + In + Fe, were found to produce even more convoluted phase combinations.

In summary, the anion-exchange-driven transformations of double perovskites performed under the present conditions resulted mostly in the decomposition of the original elpasolites and the formation of multi-phase mixtures. Detailed analysis and discussion of such mixtures go beyond the scope of the present report.

Only two cases yielded single-phase products: (i) partial Cl-to-Br exchange in $Cs_2AgBiCl_6$ perovskites[32] and (ii) conversion of CNBSC perovskites into CBS–CB and CBS–I.

The case (ii) is of special interest because it allows the application of mild anion exchanges with NaBr/NaI for the synthesis of perfectly stable double salts with independently variable M and X sites. This variability opens a large potential for the compositional design of perovskite-like double salts by using the HTP experimentation concept developed earlier for double chloride perovskites.[41] In the next sections, we focus on the exploration of the compositional landscape of $Cs_3(Bi,Sb)_2X_9$ double salts (X = Cl, Br, I, and various halide combinations). The discussion is split into two sections focusing on (i) multi-halide alloying on the X site of Bi-only compounds and (ii) on simultaneous variations of both M and X sites.

2.2 Alloying halide site – X = Cl + Br + I

The feasibility of alloying all three halides on the X site of $Cs_3Bi_2X_9$ double salts was tested using an HTP protocol similar to that discussed in our recent reports (see Experimental details in the ESI†).[41,42] In the first step, a 6 × 8 array of identical chloride precursor samples were prepared, followed by the addition of mixed NaBr + NaI solutions with different iodide/ bromide ratios. The content of NaI was increased along the X axis, while the content of NaBr was simultaneously increased along the Y axis. The concentration of NaBr and NaI is presented here as fractions, with 100% corresponding to the bromide (iodide) amount necessary for the complete stoichiometric substitution of chloride anions (ESI,† Table S1). This way, the NaI amount was varied along the X-axis from 0 to 120%, and NaBr along the Y-axis from 0 to 80%. The anion exchange was performed in the open-atmosphere environment at intense refluxing, resulting in brightly colored anion-exchange products in the form of suspensions. The suspensions were subjected to several purification cycles and used to drop-cast several sets of

films for spectroscopic and structural characterization studies (ESI,† Fig. S5).

It is noteworthy that the anion exchange with mixtures of NaBr and NaI (further denoted as NaBr/NaI) can also be performed with different chloride precursors, for example, with $Cs_3Bi_2Cl_9$ or $Cs_2AgBiCl_6$, resulting in the same $Cs_3Bi_2X_9$ (X = Cl + Br + I) products after purification (ESI,† Fig. S6). This flexibility is achieved due to the decomposition of the chloride perovskite(-like) precursor by NaI and the extraction of Ag^+ in the form of colloidal AgI, which is almost completely removed in the purification step.

Additional flexibility is provided by the HTP experimentation that allows the "geometry" of NaBr/NaI additions to be easily tuned, for example, switching from separate increments of NaI and NaBr along the X-axis and Y-axis, respectively (Fig. 1(a) and ESI,† Fig. S7a), to another regime of the variation of the NaBr/NaI ratio along the X-axis with a simultaneous increase in the total Br + I amount along the Y-axis (ESI,† Fig. S7b). With both regimes tested, we focus on the first regime of separate NaBr/NaI increments as it yields the broadest domain of single-phase $Cs_3Bi_2X_9$ products.

The $Cs_3Bi_2X_9$ sample array shown in Fig. 1(a) was studied by a combination of XRD, scanning electron microscopy (SEM), and energy-dispersive X-ray spectroscopy (EDX) for structural, morphological, and compositional characterization, respectively (see the complete set of XRD patterns in Fig. S8 (ESI†), the collection of SEM images in Fig. S9 (ESI†), the results of EDX analysis in Table S2 (ESI†), and the selected EDX spectra in Fig. S10, ESI†).

It was found that the anion exchange performed solely with NaI (series A1–A8 in Fig. 1(a)) results in the decomposition of $Cs_2AgBiCl_6$ and the formation of hexagonal CB–I double salts, with the CB–I content increasing proportionally to the amount of introduced NaI (ESI,† Fig. S11). The same observations were collected for the transformations of the $Cs_3Bi_2Cl_9$ (CB–C) precursor (data not shown), both datasets indicating that chloride and iodide cannot co-exist in the lattice of the double salts under the conditions of our experiments.

According to the combined XRD/EDX analysis, the co-introduction of NaBr and NaI results in the formation of trigonal symmetry $Cs_3Bi_2X_9$ double salts containing simultaneously all three halides, chloride, bromide, and iodide, in fractions proportional to the nominal amounts of the introduced NaBr and NaI (ESI,† Table S2). At this, a compositional domain exists where the content of $Cs_3Bi_2(Cl, Br, I)_9$ phase, or CB–CBI, exceeds 90%. This domain is marked as unblurred in Fig. 1(a) (further referred to as the "CB–CBI domain") and corresponds to the "red" area on the compositional map presented in Fig. 1(b), showing samples with more than 90% of the single-phase CB–CBI.

SEM photographs of the array presented in Fig. 1(a) showed no specific differences in morphology among the samples, all being randomly aggregated polycrystalline solids with a broad grain size distribution and a tendency to form plate- or tablet-shaped crystals (ESI,† Fig. S9).

For each particular NaBr content, the elementary cell volume of CB–CBI increases proportionally to the nominal
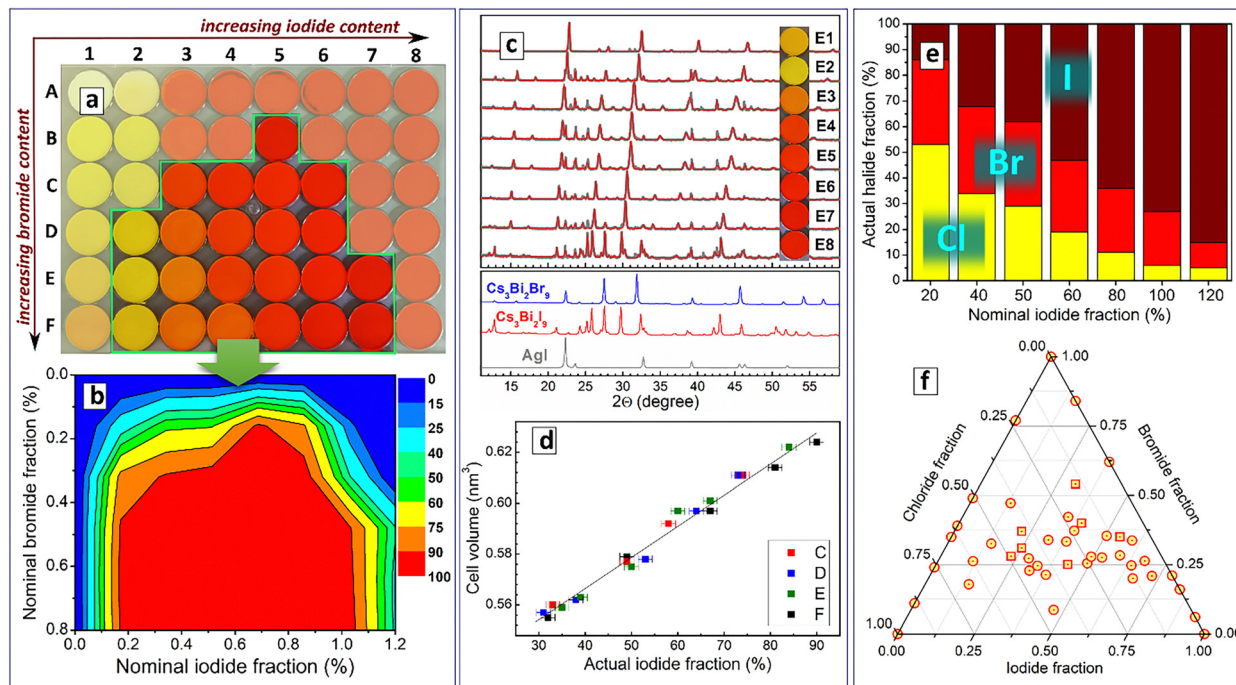
Fig. 1 (a) Photograph of the sample array produced by anion-exchange of $Cs_2AgBiCl_6$ with NaBr/NaI mixtures. (b) Distribution map of the single-phase trigonal symmetry CB–CBI double salts, with the colors from blue to red indicating a gradual increase of the CB–CBI phase content from zero to above 90%. The "red" single-phase area on the map corresponds to the unblurred area in Fig. 1(a). (c) Exemplary powder XRD patterns of anion exchange products in series E. (d) Elementary cell volume of the CB–CBI double salts as a function of the actual iodide fraction in series C–F. (e) Exemplary dependence of actual Cl, Br, and I fractions on the nominal iodide fraction in series E. (f) Summary of the composition of halide components for all single-phase samples of trigonal symmetry CB–CBI double salts. Circles correspond to the samples from the main sample array (Fig. 1(a) and ESI,† Fig. S7a), and squares to the samples from the auxiliary sample array (ESI,† Fig. S7b).

NaI content (ESI,† Table S2), as exemplified by the evolution of XRD patterns in series E (Fig. 1(c)). In general, within the single-phase CB–CBI domain, the elementary cell volume is directly proportional to the actual iodide content (Fig. 1(d)).

The co-existence of chloride, bromide, and iodide in the lattice of CB–CBI double salts is illustrated in Fig. 1(e), showing a distribution of halide fractions for the exemplary series E. As the content of both NaBr and NaI increases, the relative content of chloride decreases from *ca.* 50% to a mere 5%, the relative iodide content increases from *ca.* 15% to 85%, and the bromide content is reduced from *ca.* 40% to 10% (Fig. 1(e)). Similar distributions were collected for the entire CB–CBI domain (ESI,† Table S2).

It should be noted that the combination of all three halides in a single perovskite phase is far from being a trivial phenomenon. Within the space of lead-free perovskites, it was only reported for $MASn(Cl,Br,I)_3$ at Br fractions higher than 50%.[43] Similar to our observations, $MASn(Cl,Br)_3$ and $MASn(Br,I)_3$ compounds could be produced, while $MASn(Cl,I)_3$ alloys are unstable due to a large difference in ionic radii between chloride and iodide.[43]

It is noteworthy that all CB–CBI compounds with triple halide components crystallize in the trigonal symmetry (space group $P3m1$), typical for $Cs_3Bi_2Cl_9$ and $Cs_3Bi_2Br_9$, even at the lowest bromide contents, unlike $Cs_3Bi_2I_9$, which crystallizes as a hexagonal symmetry phase (space group $P6_3/mmc$). A similar

trend was also observed for $Cs_3Bi_2(Br,I)_9$ or CB–BI double salts, as discussed in the next section, which also form trigonal symmetry phases for any bromide contents (ESI,† Table S7). These observations indicate that bromide plays the role of a structure-directing agent, dictating the trigonal symmetry of CB–CBI and CB–BI salts. Simultaneously, bromide balances the large difference in ionic radii between chloride and iodide and allows all three halides to co-exist in the single-phase CB–CBI compounds.

Another prominent feature of CB–CBI double salts is the presence of chloride in all samples, even those produced with nominal excesses of NaBr and/or NaI, indicating an incomplete character of the anion exchange at any given NaBr/NaI contents. Similarly, the incomplete character of the bromide-to-iodide substitution was observed for CB–BI double salts, as discussed in the next section. Considering that the present synthetic protocols are based on spontaneous reactions and ionic equilibria with a minimal thermal input, these observations can be interpreted in terms of higher stability of mixed-halide compounds, as compared to less complex counterparts.

An increase in the NaBr content without NaI (Fig. 1(a), series $x1$, x = A...F) results in the conversion of the $Cs_2AgBiCl_6$ precursor into a series of $Cs_2AgBi(Cl,Br)_6$ perovskites with smoothly varied lattice parameters and band gaps (ESI,† Fig. S12), which were discussed in detail in our recent report,[32] while the $Cs_3Bi_2Cl_9$ precursor is converted into a series of solid-solution $Cs_3Bi_2(Cl,Br)_9$ (CB–CB) double salts.
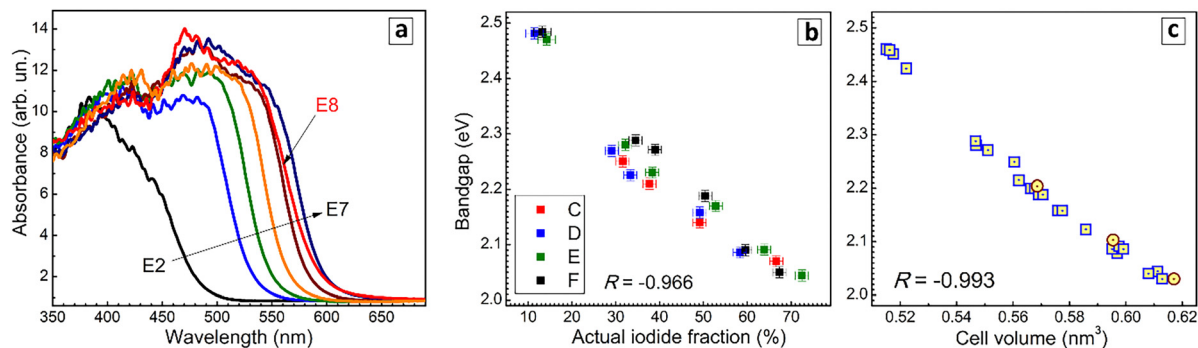
Fig. 2 (a) Exemplary absorption spectra of series E. (b) and (c) Dependences of the band gap of CB–CBI double salts on the actual iodide fraction (b) and elementary cell volume (c). Blue squares correspond to CB–CBI compounds and brown circles to CB–BI compounds.

The entire family of CB–CBI, CB–CB, and CB–BI compounds can be summarized in a ternary diagram (Fig. 1(f)), showing the compositional area of single-phase products covered by the present HTP screening campaign.

The triple-halide compounds occupy a large compositional range, from a few percent up to *ca.* 70% for chloride, from 25% up to *ca.* 90% for bromide, and *ca.* 30% up to *ca.* 90% for iodide.

Because of this compositional variability, the triple-halide CB–CBI compounds reveal the highly tunable positions of the absorption threshold (Fig. 2(a)) with the indirect band gap decreasing from *ca.* 2.5 eV down to *ca.* 2.0 eV, inversely proportional to the actual iodide fraction (Fig. 2(b)).

In general, the band gap value is dictated by the iodide content, with variations in the bromide content having only a marginal effect on the spectral characteristics of CB–CBI double salts. In line with these observations, the band gap inversely scales with the elementary cell volume (Fig. 2(c)), which is also mostly determined by the iodide content (ESI,† Table S2). This inverse dependence is general for the single-phase domain, including all triple CB–CBI and double CB–BI combinations (Fig. 2(c)).

2.3 Bi/Sb alloying – anion exchanges in chloride and bromide double salts

2.3.1 Anion exchanges in chloride double salts. As discussed in 2.1, the $Cs_3Bi_xSb_{1-x}Cl_9$ (CBS–C) double salts with a varied Bi/Sb ratio were first unintentionally produced during the HTP screening of $Cs_2Ag_xNa_{1-x}Bi_ySb_{1-y}Cl_6$ (CANBSC) perovskites as row A with $x = 0$.[41] In the present work, the CBS–C family was reproduced intentionally with the proper stoichiometry and no silver and sodium additions, showing the same composition and structural characteristics as the corresponding samples A1–A8 in the CANBSC array.

Fig. 3(a) (curve set "Cl") presents exemplary XRD profiles for CBS–C compounds with $x = 0$, 0.5, and 1.0, showing trigonal symmetry typical for CB(S)–C double salts. The EDX examination of the CBS–C compounds confirms the double salt stoichiometry, with Cs/(Bi + Sb) close to 1.5 and Cl/(Bi + Sb) close to 4.5, and shows good correspondence between the nominal and actual Bi fractions (Table 1 and ESI,† Table S3).

The elementary cell volume of CBS–C compounds is growing linearly with the actual Bi fraction, as typical for ideal solid solutions (Fig. 3(b), scatter 1 and Table 1).
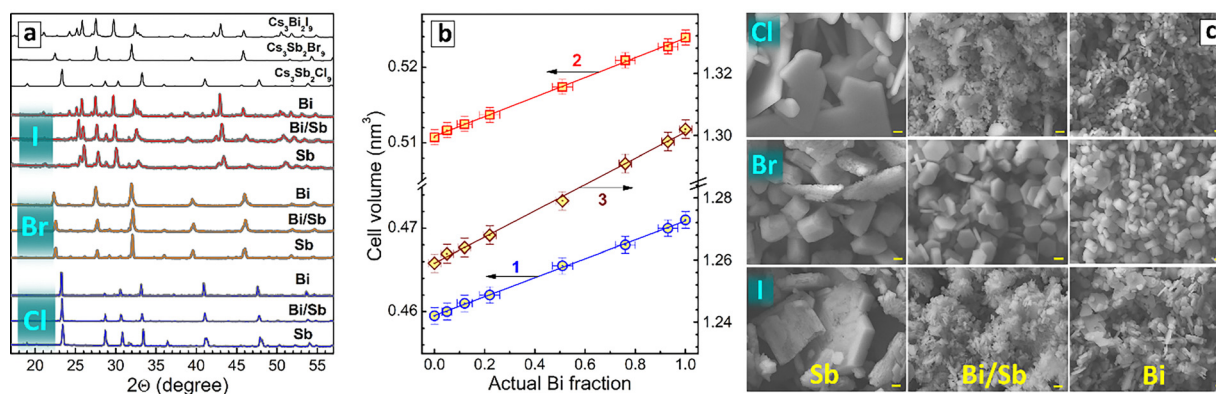

Fig. 3 (a) Exemplary powder XRD profiles (gray lines) of CBS–C double salts (designated as "Cl") and the products of their anion exchanges with NaBr ("Br") and NaI ("I"); the bismuth fraction is 0 for "Sb", 0.5 for "Bi/Sb" and 1.0 for "Bi". Thin blue/orange/red lines represent the results of Rietveld refinement using reference structures presented in the upper part by black lines. (b) Elementary cell volume V_c for CBS–X double salts as a function of the actual Bi fraction v_{Bi}. X = Cl (scatter 1), Br (scatter 2), and I (scatter 3). Solid lines represent linear fits: $V_c = 459.6 + 11.1v_{Bi}$ (scatter 1), $V_c = 511.1 + 13.2v_{Bi}$ (scatter 2), and $V_c = 1259.1 + 42.2v_{Bi}$ (scatter 3). (c) Exemplary SEM images of CBS–X double salts, X = Cl, Br, or I, with the bismuth fractions of 0 ("Sb"), 0.5 ("Bi/Sb"), and 1.0 ("Bi"). Scale bar is 1 μm.

Table 1 Summary of the characteristics of CBS–X samples with X = Cl, Cl + Br, and I: stoichiometry, actual Bi fraction x, lattice symmetry, elementary cell volume $V_{CBS–X}$, and band gap E_g

X	M	X/M	Cs/M	Symmetry, $V_{CBS–X}$ (Å^3)	E_g (eV)
Cl	Bi	4.3	1.4	Trigonal, 471.2	3.10
	Bi + Sb ($x = 0.50$)	4.3	1.5	Trigonal, 465.5	2.83
	Sb	4.3	1.5	Trigonal, 459.5	2.96
Cl + Br	Bi	4.3	1.6	Trigonal, 523.9	2.67
(ca. 25% Cl)	Bi + Sb ($x = 0.54$)	4.4	1.4	Trigonal, 517.4	2.47
	Sb	4.5	1.6	Trigonal, 510.7	2.58
I	Bi	4.5	1.5	Hexagonal, 1302	2.11
	Bi + Sb ($x = 0.46$)	4.2	1.5	Hexagonal, 1279	2.01
	Sb	4.3	1.5	Hexagonal, 1259	2.03

Notes: the accuracy is 0.1, 0.1, 0.1, 0.01, and 0.01 for X/M, Cs/M, $V_{CBS–X}$, E_g, and x, respectively.

The morphology of CBS–C salts depends noticeably on composition, evolving from *ca.* 1 μm octahedral and plate-shaped crystals for CB–C to larger CS–C platelets through an intermediate mixed morphology for CBS–C (Fig. 3(c), panel "Cl").

The products of anion exchange with the stoichiometric amount of NaBr retain the trigonal symmetry typical for chloride and bromide double salts (Fig. 3(a), curve set "Br"), also showing linear dependence between the actual Bi fraction and the elementary cell volume (Fig. 3(b), scatter 2; and Table 1), typical for ideal solid solutions.

The Cl-to-Br exchange products also have a stoichiometry typical for the double salts (Table 1) and a good match between the nominal and actual Bi/Sb ratios (ESI,† Table S4). All compounds retain 25–30% of the original chloride content even for the samples with excessive amounts of NaBr, and, therefore, the products were designated as $Cs_3(Bi,Sb)_2(Cl,Br)_9$ or CBS–CB.

The morphology of CBS–CB compounds is different from that of the original chlorides (Fig. 3(c), panel "Br"), showing polycrystalline 1–2 μm polyhedra for CB–CB, plate-shaped crystals with a lateral size of 2–3 μm and a thickness of *ca.* 0.5 μm for CBS–CB, and diverse crystal shapes for CS–CB, including relatively large 4–6 μm polyhedra and waffle-like formations.

The anion exchange of CBS–C compounds with a stoichiometric amount of NaI converts them into hexagonal $Cs_3(Bi,Sb)_2I_9$ (denoted as CBS–I) double salts (Fig. 3(a), curve set "I"). The elementary cell volume of CBS–I increases linearly with an increment in the actual Bi fraction (Fig. 3(b), scatter 3).

The family of CBS–I compounds shows a typical stoichiometry of double salts, with good agreement between the nominal and actual Bi/Sb ratios (ESI,† Table S5). The samples of CB–I and CBS–I have a distinct plate-like crystal morphology, while CS–I reveals porous waffle-like formations, similar to CS–CB. In contrast to CBS–CB, iodide can completely substitute chloride in this case, with only residual chlorine observed in the samples.

2.3.2 Anion exchanges in bromide double salts. As shown above, the anion exchange transformations of chloride double salts with NaBr or NaBr/NaI are always incomplete under the present conditions, resulting in chloride–bromide or chloride–bromide–iodide products.

To probe the properties of pure bromide double salts and to convert them into bromide–iodide derivatives, we developed an open-atmosphere approach to $Cs_3(Bi,Sb)Br_9$ double salts (denoted as CBS–B). It is based on room temperature CBS–B precipitation at the interaction of two precursors. The first precursor contains a mixture of $BiBr_3$ and $SbBr_3$ dissolved in 2-propanol/HBr, while the second precursor provides cesium acetate in 2-propanol, the latter acting as an anti-solvent (see more experimental details in the ESI†).

The products of the precipitation (see series Ax = A1–A8 in Fig. 4(a)) show the presence of a single trigonal symmetry $Cs_3Bi_2Br_9$-like phase for all Bi/Sb ratios with no detectable admixtures of other phases (Fig. 4(c)).

Mixing of Bi^{3+} and Sb^{3+} results in a strong reduction of the grain size of CBS–B compounds as compared to individual CB–B and CS–B (Fig. 4(b), samples A1, A5, and A8), most probably due to differences in $BiBr_3$ and $SbBr_3$ reactivities and non-homogeneous character of the nucleation.

An EDX analysis of the CBS–B series revealed good correspondence between the nominal and actual Bi fractions and the stoichiometry expected for CBS–B double salts, in a particular Cs/(Bi + Sb) ratio of *ca.* 1.5 and Br/(Bi + Sb) ratio of *ca.* 4.5 (Table 2).

The elementary cell volume of CBS–B double salts grows linearly with the increase of the Bi fraction (Table 2 and Fig. 4(e), scatter 1), attesting to the solid-solution character of the products.

To perform the bromide-to-iodide anion exchange, the CBS–B series was repeatedly produced six times, resulting in an array of six identical sample rows (A–F, Fig. 4(a)). Row A was left unchanged as a reference, while increasing amounts of NaI solution were added to rows B–F, with the NaI content gradually elevated from 13% in series B to 100% in series F (Fig. 4(a) and ESI,† Table S6). Similar to the previous section, the NaI content is expressed relative to the stoichiometric amount needed for complete substitution of bromide anions.

A Rietveld refinement-based analysis of the XRD data showed that the samples produced with 13–66% NaI contain a single trigonal symmetry phase typical for CBS–B double salts, while series E and F, synthesized with higher amounts of NaI, show admixtures of the hexagonal symmetry CBS–I phase (Fig. 4(d) and ESI,† Table S7; a complete set of XRD patterns is presented in Fig. S13).

Within each of the sample rows, the elementary cell volume grows linearly with the Bi fraction (for example, row C is shown in Fig. 4(e), scatter 2). In the sample columns with the same Bi/Sb ratio and an increasing amount of NaI, the elementary cell volume shows a linear growth with the actual iodide content (for example, series A5–F5 in Fig. 4(d); also Fig. 4(e), scatter 3; Table S7; exemplary EDX spectra in Fig. S14, ESI†).

An EDX analysis of the CBS–BI array showed all samples in series B–F to be single-phase compounds with mixed M and X = Cl + Br. The actual bromide fraction decreased from 85% for series B to *ca.* 60% in series C, down to *ca.* 10% in series F (ESI,† Table S7). It is noteworthy that for every series, the variation of the Bi/Sb ratio occurs at an almost constant Br/(Br + I) ratio,
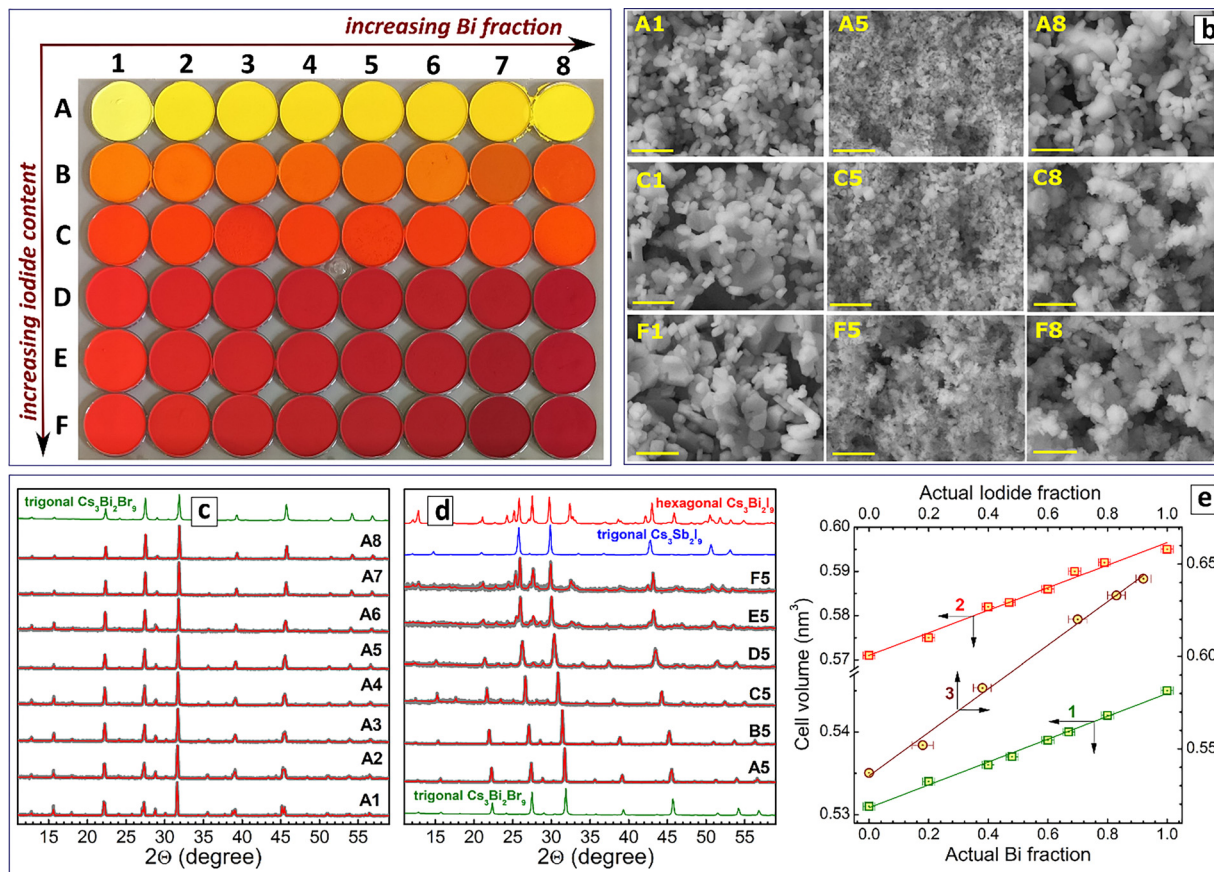
Fig. 4 (a) Photographs of the sample array of the CBS−B double salts (series A) and the products of anion exchange with NaI (series B−F). (b) Selected SEM images of the samples from the array. The scale bar is 2.5 μm. (c) and (d) Powder XRD patterns of samples in series Ax (c) and x5 (d). Gray lines represent experimental data and red lines represent the results of the Rietveld refinement. Reference patterns of trigonal symmetry $Cs_3Bi_2Br_9$ and $Cs_3Sb_2I_9$, as well as hexagonal symmetry $Cs_3Bi_2I_9$, are added as green, blue, and red solid lines, respectively. (e) Elementary cell volume V_c of series Ax (scatter 1), Cx (x = 1…8), and x5 (x = A…F) as a function of the actual Bi fraction v_{Bi} (scatter 1 and 2) and the actual iodide fraction v_I (scatter 3). Solid lines show the results of linear fitting: $V_c = 530.4 + 14.2v_{Bi}$ (scatter 1), $V_c = 571.1 + 26.3v_{Bi}$ (scatter 2), and $V_c = 538.1 + 118.2v_I$ (scatter 3).

Table 2 Composition, volume of elementary lattice cell V, and band gap E_g of CBS−B double salts

Sample ID	Bi fraction		Br/ (Bi + Sb)	Cs/ (Bi + Sb)	V, Å^3	E_g, eV
	Nominal	Actual				
A1	1.00	1.00	4.2	1.5	544.6	2.62
A2	0.80	0.80	4.1	1.5	542.7	2.52
A3	0.70	0.67	4.2	1.5	540.5	2.49
A4	0.60	0.60	4.3	1.4	539.5	2.47
A5	0.50	0.48	4.3	1.4	538.1	2.47
A6	0.40	0.40	4.3	1.4	535.9	2.45
A7	0.20	0.20	4.2	1.5	533.5	2.47
A8	0	0	4.5	1.4	530.4	2.52

Notes: the accuracy is 0.01, 0.1, 0.1, 0.1, 0.1, and 0.01 for actual Bi fraction, Br/(Bi + Sb), Cs/(Bi + Sb), V, and E_g, respectively.

indicating a reliable control over the variation of both ratios in the present synthetic protocol.

The morphology of the iodide-exchanged samples was found to mimic that of the original bromides, with intermediate Bi/Sb compounds always showing a smaller grain size as compared to Bi-only and Sb-only compounds (Fig. 4(b), samples C1−C8 and F1−F8; a complete set of SEM images in ESI,† Fig. S15).

2.3.3 Band-bowing effects in Bi/Sb double salts – the influence of the halide component. Recently, we have reported the effect of band bowing for $Cs_2AgBi_xSb_{1-x}Cl_6$ double perovskites, with the band gaps of Bi/Sb-mixed compounds being lower than those of $Cs_2AgBiCl_6$ and $Cs_2AgSbCl_6$, and the minimal E_g value observed at a Bi/Sb ratio of *ca.* 0.5.[32] This effect was also observed for the products of the anion exchanges of CABSC perovskites, in particular, CBS−CB and CBS−I,[32] showing that the band bowing phenomenon is general for different halide Bi/Sb compounds. The present campaign provided further examples of the band bowing effect in Bi/Sb halide compounds.

A set of five series of samples with the Bi/Sb ratio varied from 0 to 1 and different halide components were selected to evaluate the effect of the halide component on the bowing parameters. The set includes CBS−C (ESI,† Table S3), CBS−CB (25–30% chloride; ESI,† Table S4), CBS−B (Table 1), CBS−BI (*ca.* 60% bromide; ESI,† Table S7, series C), and CBS−I (ESI,† Table S5). All these series show visual signs of the band bowing,

the Bi/Sb-mixed samples having relatively deeper coloration as compared to individual compounds (Fig. 5(a)). In line with these visual observations, the absorption edge of CBS–X compounds in each series can be found at lower wavelengths than the corresponding Bi- and Sb-only compounds (Fig. 5(b)).

The band-bowing effect in $A_3(Bi,Sb)_2X_9$ compounds is well-documented.[20,21,40] Among the three most probable origins of the band-bowing in semiconductors, (i) local changes of the lattice cell parameters, (ii) local disordering, and (iii) chemical differences between the constituents, the third factor is considered to be dominating in $A_3(Bi,Sb)_2X_9$ double salts.[21,40] Both the valence band (VB) top and the conduction band (CB) bottom of Bi-pure and Sb-pure compounds are formed by combinations of metal-related and halide-related orbitals, with the corresponding antimony-centered orbitals having higher energies.[21] The energy mismatch in alloyed compounds results in the dominance of Sb-related orbitals in VB and Bi-related orbitals in CB, resulting in a net narrowing of the band gap of mixed compounds, as compared to the individual halides.[21,40]

Typically, the band-bowing effects in $A_3(Bi,Sb)_2X_9$ compounds are discussed for only a few X compositions, mostly individual Cl, Br, or I.[20,21,40] At this, the comparison of different reports is far from being straightforward due to differences in the sample histories. Here, we have the unique opportunity to track the band bowing for the entire range of Bi/Sb ratios and a large set of different halide combinations on the X site, with all the samples produced in very similar and thermodynamically equilibrated conditions.

According to our recent observations,[32] the absorption spectra of $Cs_2Ag(Bi,Sb)Cl_6$ perovskites and their anion-exchanged derivatives can be presented in the Tauc coordinates for both direct and indirect interband transitions. In both bases, the

Tauc derivatives show reasonably large linear sections of the absorption edge available for accurate determination of both indirect and direct band gaps (see some examples in the ESI,† Fig. S16 and Table S8). Because of this uncertainty, we analyzed the evolution of indirect band gaps as a more general case (see complete sets of values presented in the ESI,† Tables S2–S5, S7).

Fig. 5(c) shows collections of the band gaps as functions of the actual Bi fraction for the selected set of five representative CBS–X families, all of them revealing distinct band-bowing behavior. The shape of these dependencies can be presented as $E_g(CBS–X) = xE_g(CB–X) + (1 - x)E_g(CS–X) - Bx(1 - x)$, where x is the molar fraction of bismuth and B is a bowing parameter.[20,21]

The compositional dependences of the band gap show different curvatures for different CBS–X compounds (Fig. 5(c)), higher for chloride-containing compounds and lower for bromide- and iodide-containing double salts. These differences indicate the compositional dependence of the bowing parameter.

Fitting of the experimental data by fitting with the above equation (see fitting curves in ESI,† Fig. S17) showed that the bowing coefficient B indeed depends considerably on the composition of the halide component of Bi/Sb double salts. It decreases from ca. 0.8 eV for the pure chloride CBS–C family to ca. 0.6 eV for mixed CBS–CB compounds and further to 0.45–0.40 eV for double salts containing bromide and iodide (Fig. 5(d)).

This observation is in agreement with the broadly accepted assumption that the band-bowing phenomena in complex Bi/Sb halides originate from the chemical differences between the samples, rather than the local disordering or strains induced by unequal ionic sizes, octahedral tilting, or distortion of the structural units.[21,40] The main contribution of the present study is the opportunity to observe the development of the band bowing on a
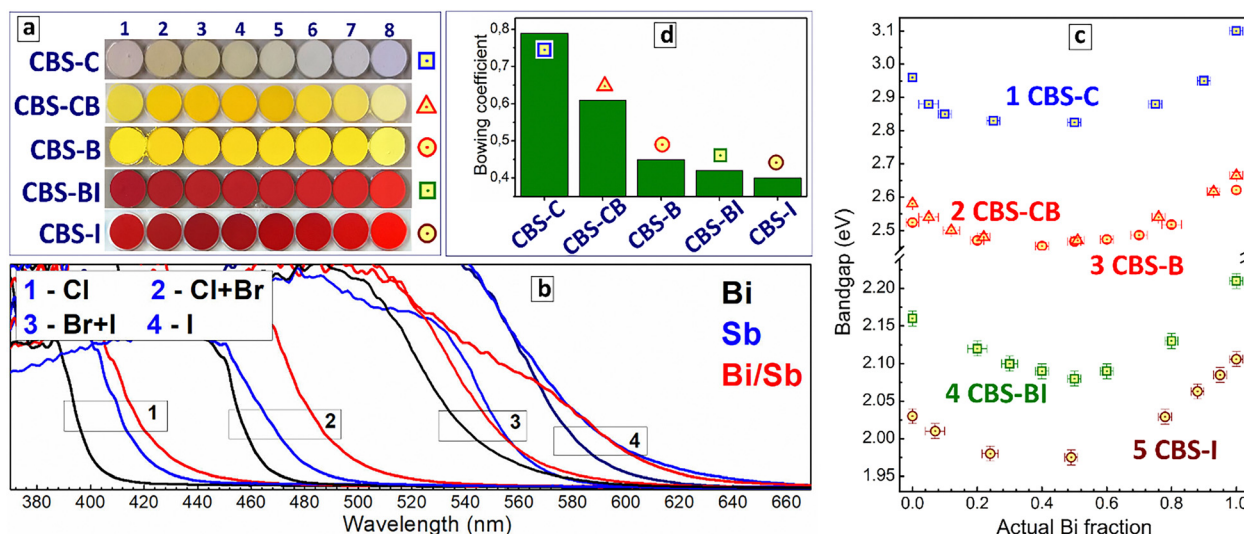

Fig. 5 (a) A collection of photographs of CSB−X double salts. Bismuth fraction is 0 (1), 0.05 (2), 0.10 (3), 0.25 (4), 0.50 (5), 0.75 (6), 0.90 (7), and 1.00 (8) for X = Cl, Cl + Br, and I; 0 (1), 0.1 (2), 0.2 (3), 0.4 (4), 0.5 (5), 0.6 (6), 0.8 (7), and 1.0 (8) for X = Br, Br + I. (b) Absorption spectra of CBS−X with X = Cl (box 1), X = Cl + Br (box 2), X = Br + I (box 3), and X = I (box 4); Bi fraction is 1.0 (black lines), 0 (blue lines), and 0.5 (red lines). (c) Band gap dependences of CBS−X samples on the actual Bi fraction for X = Cl (1), Cl + Br (2), Br (3), Br + I (4), and I (5). (d) Band bowing coefficient (expressed in eV) for different CBS−X double salts.

much broader range of samples with a broader variety of halide compositions than typically reported.

3 Conclusions

A high-throughput compositional screening of perovskite-like $Cs_3M_2X_9$ double salts, where M = Bi and Sb, and X = Cl, Br, and I, was performed, with independent variations of the metal M and halide X compositions. The screening was based on a combination of mild room-temperature open-atmosphere engineered precipitation of chloride and bromide precursors and their conversion into more complex halide derivatives by mild anion-exchange with NaBr/NaI.[32]

First, the variation of the X position was performed at a fixed M = Bi^{3+} and yielded a set of 44 single-phase $Cs_3Bi_2X_9$ compounds with X = Cl, Cl + Br, Br, Br + I, and Cl + Br + I.

The Cl-for-Br anion exchange resulted in trigonal symmetry $Cs_3Bi_2(Cl,Br)_9$ double salts, while the Cl-to-I exchange yielded hexagonal symmetry $Cs_3Bi_2I_9$ in all cases, indicating incompatibility of chloride and iodide anions in the double salt lattice under the present conditions.

In contrast, the anion exchange of chloride with combinations of Br and I was found to produce stable $Cs_3Bi_2X_9$ compounds with all three halides simultaneously present in the lattice, that is, X = Cl + Br + I. These compounds represented a dominating phase in a relatively large compositional area with Cl, Br, and I contents varied in the ranges of *ca.* 40–90%, 10–60%, and 30–90%, respectively.

All bromide-containing double salts (X = Cl + Br and Cl + Br + I) showed the same space symmetry group, even at the lowest Br contents, indicating that the bromide not only enables the co-existence of Cl and I in the same phase, but also dictates the trigonal symmetry of mixed-halide compounds.

The CB–CBI compounds showed a band gap variation in the range of *ca.* 2.0–2.5 eV, with linear dependences of the band gap on the iodide fraction and the elementary cell volume.

In the second step, the anion-exchange-based engineering of the X site was combined with variations of the M site by alloying Bi^{3+} and Sb^{3+} cations.

To enable the HTP screening of CBS–B and CBS–BI compounds, a new mild open-atmosphere protocol for the engineered precipitation of single-phase trigonal symmetry $Cs_3(Bi,Sb)_2Br_9$ double salts was introduced, allowing the bromo–iodide CBS–BI family to be produced by the anion exchange with NaI. This double-site screening yielded a total of 56 single-phase solid-solution CBS–X compounds with X = Cl, Br, I, Cl + Br, and Br + I, and the Bi/Sb ratio varied from 0 to 1.0.

In all cases, the CBS–X families revealed a band bowing effect, with the band gaps of mixed Bi/Sb compounds being lower than the band gaps of individual Bi-only and Sb-only counterparts. The bowing parameter was found to depend on the composition of the halide sub-system, decreasing from 0.80 eV for chlorides to 0.60 eV for chloro-bromides and down to 0.40–0.45 eV for bromides and bromo-iodides. This trend indicates that chemical variations in the mixed Bi/Sb lattices,

rather than local disorders or lattice strains, are the main reasons for the band-bowing behavior.

In general, the present observations show high potential for band gap engineering in complex Bi/Sb perovskites and perovskite-like materials by simultaneous compositional tuning of both cationic and anionic subsystems.

Author contributions

O. Stroyuk: conceptualization (lead) and writing – original draft preparation (lead); O. Raievska: investigation (lead), methodology (lead), and writing – review and editing (equal); S. Kinge: project administration (lead), conceptualization (equal), and writing – review and editing (equal); J. Hauch: project administration (equal) and writing – review and editing (equal); C. J. Brabec: conceptualization (equal), funding acquisition (lead), and writing – review and editing (equal).

Data availability

The data supporting this article have been included as part of the ESI.†

Conflicts of interest

There are no conflicts to declare.

References

1 O. Almora, G. C. Bazan, C. I. Cabrera, L. A. Castriotta, S. Erten-Ela, K. Forberich, K. Fukuda, F. Guo, J. Hauch, A. W. Y. Ho-Baillie, T. J. Jacobsson, R. A. J. Janssen, T. Kirchartz, R. R. Lunt, X. Mathew, D. B. Mitzi, M. K. Nazeeruddin, J. Nelson, A. F. Nogueira, U. W. Paetzold, B. P. Rand, U. Rau, T. Someya, Ch Sprau, L. Vaillant-Roca and C. J. Brabec, *Adv. Energy Mater.*, 2025, **15**, 2404386.

2 P. K. Nayak, S. Mahesh, H. J. Snaith and D. Cahen, *Nat. Rev.*, 2019, **4**, 269.

3 W. Yu, Y. Zou, H. Wang, S. Qi, C. Wu, X. Guo, Y. Liu, Z. Chen, B. Qu and L. Xiao, *Chem. Soc. Rev.*, 2024, **53**, 1769.

4 S. Jiang, M. Liu, D. Zhao, Y. Guo, J. Fu, Y. Lei, Y. Zhang and Z. Zheng, *Phys. Chem. Chem. Phys.*, 2024, **26**, 4794.

5 L. A. Muscarella and E. M. Hutter, *ACS Energy Lett.*, 2022, **7**, 2128.

6 Y. Gao, Y. Pan, F. Zhou, G. Niu and C. Yan, *J. Mater. Chem. A*, 2021, **9**, 11931.

7 X. He, Y. Deng, D. Ouyang, N. Zhang, J. Wang, A. A. Murthy, I. Spanopoulos, S. M. Islam, Q. Tu, G. Xing, Y. Li, V. P. Dravid and T. Zhai, *Chem. Rev.*, 2023, **123**, 1207.

8 W. Li, Y. Liu, X. Huang, S. Jiang, C. Zhao and W. Mai, *ACS Appl. Mater. Interfaces*, 2021, **13**, 53194.

9 S. Tie, X. Lu, G. Tang, W. Tian, P. Lin, J. Zhu, W. Huang and X. Zheng, *J. Phys. Chem. C*, 2025, **129**, 2260.

10 A. Pradhan, M. K. Jena and S. L. Samal, *ACS Appl. Energy Mater.*, 2022, **5**, 6952.

11 M. Singh, Akash and J. P. Tiwari, *ACS Appl. Energy Mater.*, 2024, **7**, 10212.

12 Y. J. Li, B. H. Mu, H. B. Li, S. C. Tang, J. Tian, Y. Li, Z. Y. Ji, Y. J. Wang, T. He, A. V. Emeline, D. W. Bahnemann and J. H. Pan, *Energy Fuels*, 2025, **39**, 2986.

13 J. Lee, W. K. Chong, S. H. W. Kok, B. J. Ng, X. Y. Kong, S. P. Chai and L. L. Tan, *Adv. Funct. Mater.*, 2023, **33**, 2303430.

14 A. A. Cepeda-Aguirre, B. I. Kharisov, L. M. Torres-Martínez and E. Luevano-Hipolito, *Sol. Energy*, 2025, **288**, 113296.

15 A. Yadav, A. Saini, P. Kumar and M. Bag, *J. Mater. Chem. C*, 2024, **12**, 197.

16 S. Li, J. Qian, J. Ma and X. Zhang, *CrystEngComm*, 2024, **26**, 6545.

17 Y. Wang, Q. Ran, T. Chen, W. Zhang and K. Zhang, *J. Phys. Chem. Lett.*, 2025, **16**, 3177.

18 Z. Dong, H. Moutaabbid, Y. Chen, L. Zhang, Z. Cao and C. Liu, *J. Phys. Chem. Lett.*, 2024, **15**, 12471.

19 M. Leng, Z. Chen, Y. Yang, Z. Li, K. Zeng, K. Li, G. Niu, Y. He, Q. Zhou and J. Tang, *Angew. Chem., Int. Ed.*, 2016, **55**, 15012.

20 S. Chatterjee, J. Payne, J. T. S. Irvine and A. J. Pal, *J. Mater. Chem. A*, 2020, **8**, 4416.

21 S. Dai, X. Gan, K. Li, Q. Huang, L. Guo and H. Liu, *Phys. Chem. Chem. Phys.*, 2023, **25**, 30993.

22 H. Hashimoto, R. Oka, T. Hayakawa and C. Brabec, *Phys. Status Solidi RRL*, 2024, **18**, 2300241.

23 H. Jiang, S. Cui, Y. Chen and H. Zhong, *Nano Select*, 2021, **2**, 2040.

24 K. Sandeep, K. Padmakumar, K. U. Ambili, P. Jishnu, K. H. Fousia, A. R. Ramesh, J. P. Rappai, V. Santhi and M. Shanthil, *Phys. Status Solidi B*, 2022, **259**, 2100600.

25 J. A. Steele, M. Lai, Y. Zhang, Z. Lin, J. Hofkens, M. B. J. Roeffaers and P. Yang, *Acc. Mater. Res.*, 2020, **1**, 3.

26 Q. A. Akkerman, V. D'Innocenzo, S. Accornero, A. Scarpellini, A. Petrozza, M. Prato and L. Manna, *J. Am. Chem. Soc.*, 2015, **137**, 10276.

27 S. E. Creutz, E. N. Crites, M. C. De Siena and D. R. Gamelin, *Chem. Mater.*, 2018, **30**, 4887.

28 T. Elmelund, R. A. Scheidt, B. Seger and P. V. Kamat, *ACS Energy Lett.*, 2019, **4**, 1961.

29 S. E. Creutz, E. N. Crites, M. C. De Siena and D. R. Gamelin, *Nano Lett.*, 2018, **18**, 1118.

30 K. Gahlot, J. Meijer and L. Protesescu, *Nanoscale*, 2024, **16**, 5177.

31 A. Kumar, S. K. Swami, S. S. Rawat, V. N. Singh, O. P. Sinha and R. Srivastava, *Int. J. Energy Res.*, 2021, **45**, 16769.

32 O. Stroyuk, O. Raievska, A. Barabash, R. W. Hooper, V. K. Michaelis, J. Hauch and C. J. Brabec, *J. Mater. Chem. C*, 2024, **12**, 533.

33 S. Jiang, R. Huang, W. Li, X. Huang, H. Sheng, F. Wu, Y. Lv, Y. Fu, C. Zhao and W. Mai, *ACS App. Mater. Interfaces*, 2022, **14**, 26279.

34 D. Shen, X. Wang, X. Zhang, Y. Liu, Y. Shi, X. Li, X. Chen and Y. Zhang, *ACS Appl. Opt. Mater.*, 2023, **1**, 435.

35 C. W. Ahn, J. H. Jo, J. S. Choi, Y. H. Hwang, I. W. Kim and T. H. Kim, *Adv. Eng. Mater.*, 2023, **25**, 220119.

36 Y. Lou, M. Fang, J. Chen and Y. Zhao, *Chem. Commun.*, 2018, **54**, 3779.

37 R. F. Ali, I. Andreu and B. D. Gates, *Nanoscale Adv.*, 2019, **1**, 4442.

38 C. Guhrenz, A. Benad, C. Ziegler, D. Haubold, N. Gaponik and A. Eychmüller, *Chem. Mater.*, 2016, **28**, 9033.

39 A. Singh, N. C. Chiu, K. M. Boopathi, Y. J. Lu, A. Mohapatra, G. Li, Y. F. Chen, T. F. Guo and C. W. Chu, *ACS Appl. Mater. Interfaces*, 2019, **11**, 35088.

40 G. Giovilli, B. Albini, V. Grisci, S. Bonomi, M. Moroni, E. Mosconi, W. Kaiser, F. De Angelis, P. Galinetto and L. Malavasi, *J. Mater. Chem. C*, 2023, **11**, 10282.

41 O. Stroyuk, O. Raievska, M. Daum, J. Hauch and C. J. Brabec, *J. Mater. Chem. C*, 2024, **12**, 8705.

42 O. Stroyuk, O. Raievska, M. Daum, C. Kupfer, A. Osvet, J. Hauch and C. J. Brabec, *J. Mater. Chem. C*, 2025, **13**, 2303.

43 C. M. Tsai, N. Mohanta, C. Y. Wang, Y. P. Lin, Y. W. Yang, C. L. Wang, C. H. Hung and E. W. G. Diau, *Angew. Chem., Int. Ed.*, 2017, **56**, 13819.